Structural Basis for Herbicidal Inhibitor Selectivity Revealed by Comparison of Crystal Structures of Plant and Mammalian 4-Hydroxyphenylpyruvate Dioxygenases‡

Cheng Yang,[⊥] James W. Pflugrath,[⊥] Debra L. Camper,[§] Mendy L. Foster,[§] Daniel J. Pernich,[§] and Terence A. Walsh*,[§]

Rigaku/MSC Inc., 9009 New Trails Drive, The Woodlands, Texas 77381, and Dow AgroSciences, 9330 Zionsville Road, Indianapolis, Indiana 46268

Received April 6, 2004; Revised Manuscript Received June 2, 2004

ABSTRACT: A high degree of selectivity toward the target site of the pest organism is a desirable attribute for new safer agrochemicals. To assist in the design of novel herbicides, we determined the crystal structures of the herbicidal target enzyme 4-hydroxyphenylpyruvate dioxygenase (HPPD; EC 1.13.11.27) from the plant *Arabidopsis thaliana* with and without an herbicidal benzoylpyrazole inhibitor that potently inhibits both plant and mammalian HPPDs. We also determined the structure of a mammalian (rat) HPPD in complex with the same nonselective inhibitor. From a screening campaign of over 1000 HPPD inhibitors, six highly plant-selective inhibitors were found. One of these had remarkable (>1600-fold) selectivity toward the plant enzyme and was cocrystallized with *Arabidopsis* HPPD. Detailed comparisons of the plant and mammalian HPPD−ligand structures suggest a structural basis for the high degree of plant selectivity of certain HPPD inhibitors and point to design strategies to obtain potent and selective inhibitors of plant HPPD as agrochemical leads.

Many biochemical target sites that are useful for the design of new and improved agrochemicals occur in both the pest species (a weed, fungus, or insect) and vertebrates. Thus there is the potential for undesirable mammalian toxicological effects through inhibition of the nontarget enzyme. This has often been alleviated by exploiting differences in metabolism of the agrochemical in mammals or by carefully limiting exposures to the agrochemical. The advent of detailed structural information on the molecular target sites of agrochemicals now allows rational target site-based approaches to improving both selectivity and potency toward the pest species and away from nontarget organisms. One enzyme that is potentially amenable to such an approach is 4-hydroxyphenylpyruvate dioxygenase (HPPD[1]), the target site for recently commercialized herbicides such as isoxaflutole and mesotrione and therefore of great interest for the design of novel herbicides (*1*, *2*).

HPPD catalyzes the oxygenation of 4-hydroxyyphenylpyruvate (HPPA) to form homogentisate (HGA) with the concomitant release of CO_2 (Scheme 1). The enzyme is found in microbes, mammals, and plants and has differing functions in various organisms. In mammals, the enzyme has an important role in the catabolism of tyrosine. Deficiency of the enzyme in humans causes type III tyrosinemia, a rare autosomal recessive disorder characterized by elevated serum tyrosine levels, neurological symptoms, and mental retardation (*3*−*6*). Inhibitors of HPPD have found use as drugs for the treatment of type I tyrosinemia by blocking the formation of toxic catabolites derived from tyrosine in this disease condition (*7*). In plants, HGA formed by the action of HPPD is utilized as the aromatic precursor for tocopherols and plastoquinone (*8*). Plastoquinone is the redox cofactor for phytoene desaturase, a key enzyme in the biosynthesis of photoprotectant carotenoids (and itself the target of commercial herbicides such as norflurazon). Thus inhibition of plant HPPD prevents the normal functioning of phytoene desaturase in the synthesis of carotenoids (*1*). The loss of these essential photoprotectants results in the intense and characteristic bleaching of new plant growth by application of HPPD inhibitor herbicides, leading to plant death.

HPPDs are non-heme Fe^{2+}-dependent dioxygenases that are mechanistically related to α-ketoglutarate-dependent dioxygenases such as proline hydroxylase and clavaminate synthase (*9*). In HPPDs, the α-ketoacid moiety is contained within the substrate as the acidic side chain of HPPA. The catalyzed reaction is mechanistically complex involving an oxidative decarboxylation, alkyl group ring migration (an NIH shift), and ring hydroxylation (*10*). The crystal structure of an HPPD from *Pseudomonas fluorescens* has been

‡ Atomic coordinates of the HPPD complexes have been deposited in the Protein Data Bank (ID codes 1SQD, 1SQI, 1TFZ, 1TG5).

* To whom correspondence should be addressed. E-mail: tawalsh@dow.com. Telephone: 317-337-3680.

⊥ Rigaku/MSC Inc.

§ Dow AgroSciences.

[1] Abbreviations: HPPD, 4-hydroxyphenylpyruvate dioxygenase; HPPA, 4-hydroxyphenylpyruvate; HGA, homogentisate; *At*HPPD, *Arabidopsis thaliana* HPPD; *Rn*HPPD, *Rattus norvegicus* HPPD; *Pf*HPPD, *Pseudomonas fluorescens* HPPD; *At*HPPD−869 or *Rn*-HPPD−869, *At*HPPD or *Rn*HPPD in complex with DAS869; *At*HPPD−645, *At*HPPD in complex with DAS645; MIR, multiple isomorphous replacement.

10.1021/bi049323o CCC: $27.50
Published on Web 07/20/2004

Scheme 1

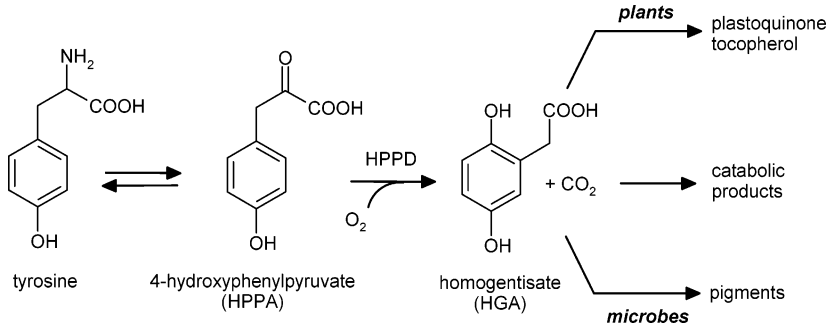

described (*11*), but this enzyme has a relatively low overall sequence homology to plant and mammalian HPPDs (21% and 29% amino acid identity, respectively). However, sequence alignments of HPPDs from a wide variety of sources show that 27 residues among more than 350 residues are completely conserved in these and all other HPPDs. The crystal structures of HPPDs from the plants *Arabidopsis thaliana* and *Zea mays* have also recently been reported (*12*). However, no HPPD structures have as yet been described that contain substrate analogues or inhibitors that could be useful for herbicide or drug design.

Several classes of potent HPPD inhibitors have been described, and all contain a 1,3-diketone moiety in some form (*13*−*15*), examples of which are shown in Figure 1. Kinetic analyses of potent HPPD inhibitors show that they exhibit the characteristics of slow, tight-binding inhibitors (*16*−*19*). The majority of HPPD inhibitors effectively inhibit both plant and mammalian HPPDs; indeed, early investigations of HPPD inhibitors benefited from observations of the physiological effects of HPPD inhibition in both plants and mammals (*20*, *21*). We were interested in understanding the structural basis for potent inhibition of the plant enzyme by herbicidal benzoylpyrazoles and in investigating possible modes of selectivity for the plant enzyme versus the mammalian enzyme for herbicide design. Accordingly, we have now determined the crystal structures of both plant and mammalian enzymes in complex with novel selective and nonselective ligands.

EXPERIMENTAL PROCEDURES

HPPD Purification. *At*HPPD and *Rn*HPPD were cloned via polymerase chain reaction amplification from appropriate cDNA libraries and overexpressed in *Escherichia coli* using the T7 expression system (*22*). Purification and N-terminal amino acid sequencing of native HPPD from maize seedlings indicated that the N-terminus was Ala23 (unpublished data). For expression of the recombinant *Arabidopsis* enzyme in *E. coli*, the sequence was therefore truncated by 21 amino acid residues at the N-terminus relative to the coding sequence of the full-length cDNA so that it was equivalent to that of a native plant enzyme.

Cells from 2 L cultures were suspended in 100 mL of 100 mM Tris-HCl, pH 7.3, containing 1 mg/mL lysozyme, 1 mM EDTA, and 150 mM sodium chloride. DNase and $MgCl_2$ were then added to final concentrations of 0.02 mg/mL and 2 mM, respectively. The lysed cells were centrifuged at 17 000*g* for 20 min, and protein was precipitated with 50% saturated ammonium sulfate for *At*HPPD. For *Rn*HPPD, the protein fraction precipitating between 35% and 70% ammonium sulfate was used. After centrifugation, the pellet was resuspended in 20 mM Tris-HCl, pH 7.3, and dialyzed overnight against two changes of 3 L of 20 mM Tris-HCl, pH 7.3. The dialyzed extract was centrifuged to clarify and applied to a Pharmacia MonoQ 10/10 column equilibrated in 20 mM Tris-HCl, pH 7.3. For *At*HPPD, the column was eluted over 60 min using a 0−60% gradient of 20 mM Tris-

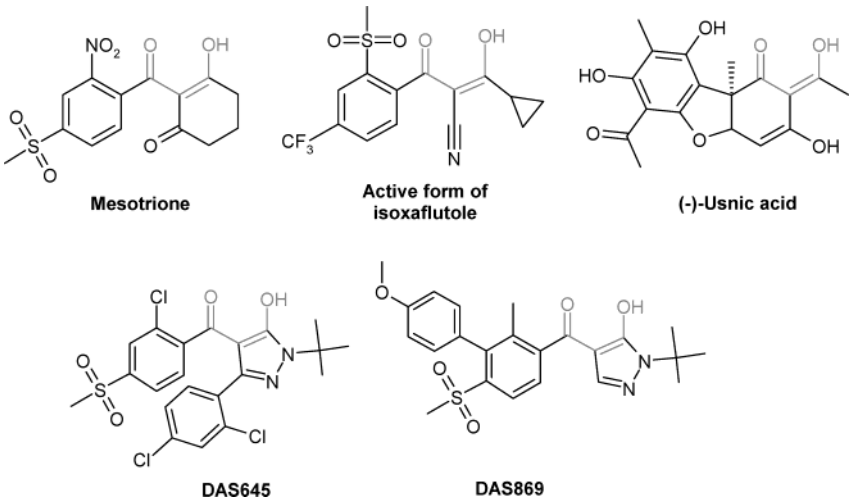

FIGURE 1: Examples of various structural classes of HPPD inhibitors. The 1,3-diketone moiety present in all potent HPPD inhibitors is shaded. Mesotrione and the diketonitrile form of isoxaflutole are commercial herbicides, (−)-usnic acid is a natural product inhibitor isolated from lichen, and DAS645 and DAS869 are experimental herbicides from the Dow AgroSciences collection. DAS869 is a potent inhibitor of both plant and mammalian HPPDs, whereas DAS645 is highly selective for the plant enzyme.

HCl, pH 7.3, 0.5 M potassium chloride at a flow rate of 2 mL/min. *At*HPPD eluted from the column at approximately 200 mM potassium chloride. For *Rn*HPPD, a gradient of 0−40% 0.5 M potassium chloride over 60 min was used. The enzyme eluted from the column at ~67 mM potassium chloride. For crystallography, the HPPD fractions were concentrated, applied to two Pharmacia Superose 12 columns connected in series, and concentrated to 20−30 mg/mL.

The K_m values of *Arabidopsis* and rat HPPDs for HPPA were 11 and 13 μM respectively, determined using a radiometric assay protocol based on that of Secor (*23*).

HPPD Inhibitor Screen. A novel high-throughput HPPD assay was developed to rapidly screen large numbers of inhibitors. This assay coupled the formation of HGA by HPPD to the production of maleylacetoacetate via HGA dioxygenase. This results in an increase in absorbance at 330 nm that permits continuous spectrophotometric monitoring of the reaction in a microplate-based format over at least 20 min. This is particularly informative in assaying slow, tight-binding inhibitors such as the 1,3-diketone inhibitors of HPPD where reaction rates can decrease significantly during the time course of an assay (*16*, *17*). HGA dioxygenase is an excellent coupling enzyme for monitoring the HPPD reaction because it requires the same cofactors as HPPD (Fe^{2+}, ascorbate) and therefore no extra additions to the reaction mix are required.

HGA dioxygenase was partially purified from *Alcaligenes xylosoxidans* subsp. *denitrificans* (ATCC 35699). Assays were performed in 96-well plates at 30 °C using a UV/visible plate reader to monitor the formation of maleylacetoacetate at 330 nm (ϵ_{330} = 13 500 M^{-1} cm^{-1}) (*24*). The assay buffer was 0.1 M MOPS, pH 7, containing 50 μM $Fe(NH_4)_2(SO_4)_2$ and 2 mM sodium ascorbate. Before assays were conducted, HPPD and HGA dioxygenase were preequilibrated in 2× assay buffer for at least 1 h. HPPD activity was measured in an assay mix containing 100 μM HPPA and ~50 μg of HGA dioxygenase preparation using sufficient HPPD to obtain a reaction rate of ~15 mOD/min. The amount of HGA dioxygenase activity was predetermined to be in large excess of the HPPD activity to ensure that the reaction was tightly coupled (the K_m of HGA dioxygenase for HGA was 25 μM).

Compounds for screening were obtained by MDL ISIS searches of the Dow AgroSciences compound collection using a variety of 1,3-diketone substructures. Compounds were dissolved in dimethyl sulfoxide and initially screened at 1, 4, and 16 μM. Selected compounds were also assayed using a preequilibrated format in which HPPD was incubated in the presence of inhibitor for 30 min prior to addition of the appropriate amounts of HGA dioxygenase and HPPA.

Crystallization and Data Collection. Crystallization trials yielded *At*HPPD, *At*HPPD−869, *At*HPPD−645, and *Rn*-HPPD−869 crystals via hanging drop vapor diffusion at room temperature. *At*HPPD, *At*HPPD−869, and *At*HPPD−645 crystals grew in 15% poly(ethylene glycol) 4000, 22% 2-propanol, and 100 mM Bis-Tris, pH 6.0, with 16 mg/mL *At*HPPD protein in 10 mM Tris, pH 7.3, 20 mM potassium chloride, and 3 mM cobalt chloride. The complexes *At*-HPPD−869 and *At*HPPD−645 were generated by incubating *At*HPPD with the appropriate compound for a few hours before crystallization trials. Platelike crystals in monoclinic space group *C*2 with one molecule per asymmetric unit (unit cell a = 77.4 Å, b = 83.7 Å, c = 63.2 Å, and β = 102.5°) appeared after a few days. The crystals had a solvent content of 33%. Prior to data collection, the crystals were transferred into the crystallization condition with 18% (v/v) ethylene glycol instead of 22% (v/v) 2-propanol. Data collections were conducted at cryogenic temperature.

*Rn*HPPD−869 was prepared by incubation of *Rn*HPPD with DAS869 in the presence of cobalt chloride overnight. The crystals grew in 10% poly(ethylene glycol) 20000, 15% (v/v) hexanediol, and 100 mM Hepes, pH 7.0, with 16 mg/mL *Rn*HPPD−869 complex in the buffer solution of 10 mM Tris, pH 7.5, and 3 mM cobalt chloride. Small crystals formed after two weeks. A microseeding technique was used multiple times to increase the crystal size. The crystal had orthorhombic space group $P2_12_12_1$ with two molecules per asymmetric unit (unit cell a = 61.6 Å, b = 107.5 Å, and c = 133.0 Å) and 40% solvent content. *Rn*HPPD−869 crystals were readily frozen without being soaked in a cryoprotectant. The data sets were also collected at cryogenic temperatures. All data collections were carried out on 5.0 kW Rigaku RUH2R generator coupling with MSC Blue multilayer optics and R-AXIS IV++ imaging plate detector. The data were processed with d*TREK data processing program suit (*25*).

Structure Determination. *At*HPPD and *Rn*HPPD−869 structures were solved by multiple isomorphous replacement (MIR). Four heavy atom derivatives of *At*HPPD were prepared as described in Table 1. For subsequent calculation, the CCP4 program suite was utilized (*26*). The difference Patterson maps of *At*HPPD data were calculated to locate the positions of main heavy atom sites. The minor sites were found through the difference Fourier map. The initial MIR phases were calculated at 3.5 Å resolution with the program MLPHARE (*26*) and had a mean figure of merit of 0.64. MIR maps were improved through the procedures of solvent flattening and histogram matching. The modified MIR was used to build the initial model with the program O (*27*). Many different heavy atom compounds were soaked into *Rn*HPPD−869 crystals and screened. Methylmercury chloride successfully derivatized *Rn*HPPD−869 crystals, and diffraction data was used in phase determination. Due to the phase ambiguity, single isomorphous replacement phases with the figure of merit of 0.23 were too poor to produce a recognizable electron density map, but its native data collected with high redundancy (Table 1) resulted in the accurate measurement of Bijvoet differences. Three additional metal ions and 10 sulfur sites were found through the anomalous difference Fourier map calculated using the initial SIR phases. The anomalous differences of the native data were added to the phase calculation and refined as a second derivative. Ultimately, the positions of three metal ions and 10 sulfur atoms were used in the phase calculations. SIR phasing has become a typical case of MIR phasing, and the SIR phase ambiguity was easily resolved (*28*). The new MIR phases produced a well-defined electron density map with the figure of merit of 0.56.

The MIR phases were also improved through the procedures of solvent flattening, histogram matching, and density averaging. The chain tracing and sequence matching started from Trp199 and Trp200 and extended in both directions with the program O. The anomalous difference Fourier maps were generated periodically using the updated phases. The anomalous peaks of sulfur atoms served as additional tracing markers (*28*). The ligand structure was modeled on the basis

Table 1: Statistics for Data Collection and Refinement of HPPD Structures

	*At*HPPD							*Rn*HPPD-869	
		heavy atom derivative							heavy atom derivative
	native	Hg1[a]	Hg2[b]	Pt[c]	Hg1+Pt[d]	*At*HPPD-869 native	*At*HPPD-645 native	native	Hg1[e]
Data Collection Statistics									
space group	C2	C2	C2	C2	C2	C2	C2	$P2_12_12_1$	$P2_12_12_1$
resolution (Å)	1.8	2.7	2.8	2.8	2.6	1.8	1.9	2.15	3.5
unique reflns	35 991	6938	9421	9283	9171	35 505	30 159	47 734	15 286
completeness (%)[f]	98.9 (89.2)	71.5 (45.6)	98.0 (90.2)	96.0 (94.3)	97.3 (88.3)	99.9 (99.8)	98.3 (83.8)	98.4 (97.2)	99.8 (99.8)
redundancy	5.2	3.4	2.8	3.2	2.8	3.4	4.4	12.5	6.0
R_{merge} (%)[f,g]	4.1 (26.9)	7.8 (27.4)	10.0 (28.7)	6.6 (31.4)	5.2 (29.8)	4.6 (16.3)	4.8 (15.5)	6.8 (24.8)	11.5 (31.8)
Phasing Statistics									
R_{iso} (%)[h]		30.1	39.4	17.2	26.7				23.1
heavy atom sites		3	4	3	3				3
R_{cullis} (%)[i]		0.56	0.66	0.78	0.67				0.77
phasing power[j]		2.68	2.07	1.27	2.09				1.30
Refinement Statistics									
resolution limits (Å)	15.0−1.8					15.0−1.8	15.0−1.9	15.0−2.15	
R_{cryst} (R_{free}) (%)[k]	21.6 (26.6)					21.5 (28.9)	18.8 (23.4)	21.6 (27.1)	
no. of molecules per ASU	1					1	1	2	
no. of non-H protein atoms	2906					2814	2865	5560	
no. of water molecules	190					203	193	463	
no. of ligand atoms	0					31	32	62	
avg B (Å^2)									
protein	25.0					18.6	18.5	30.3	
water	31.2					27.8	23.6	35.8	
ligand						17.8	15.1	44.9	
rms deviations[l]									
bond lengths (Å)	0.025					0.012	0.003	0.019	
bond angles (deg)	0.041					1.7	0.027	0.041	

[a] Native *At*HPPD soaked in 10 mM CH_3HgCl for 1 day. [b] Native *At*HPPD soaked in saturated HgO for 2 days. [c] Native *At*HPPD soaked in 10 mM Pt[ethylene$(NH_3)_2Cl_2$] for 2 days. [d] Native *At*HPPD soaked in 10 mM CH_3HgCl for 1 day, then transferred into 10 mM Pt[ethylene$(NH_3)_2Cl_2$] for 1 day. [e] Native *At*HPPD soaked in 10 mM CH_3HgCl for 3 days. [f] Numbers given in parentheses are the given statistics for the highest resolution shell. [g] $R_{merge} = \{\sum_h\sum_i I_{h,i} - I_h/(\sum_h\sum_i I_{h,i})$, where I_h is the mean intensity of the i observations of a given reflection h. [h] R_{iso} (isomorphous difference) $= \sum||F_{ph} - F_p|/\sum F_{ph}$, where F_{ph} and F_p are the derivative and native structure factor amplitudes, respectively. [i] $R_{cullis} = \sum||F_{ph} \pm F_p| - F_{h(calcd)}|/\sum|F_{ph} \pm F_p|$ for all reflections, where $F_{h(calcd)}$ is the calculated heavy atom structure factor. [j] Phasing power is the mean value of the heavy atom structure factor amplitude divided by the lack of closure for isomorphous differences. [k] $R_{cryst} = \sum_h||F_o| - |F_c||/\sum_h|F_o|$, where F_o and F_c are observed and calculated structure factor amplitudes. R_{free} is the same as R_{cryst} for 10% of the data randomly omitted from refinement. [l] The rms deviations for bond lengths and bond angles are the rms deviation for ideal stereochemical values.

of inspection of $2F_o - F_c$ and $F_o - F_c$ electron density maps and anomalous difference Fourier maps. The structures of *At*HPPD and *Rn*HPPD−869 were refined with the program REFMAC including the refinement of rigid-body, overall-*B* factors and individual *B*-factors, closely monitored by the behavior of the R_{free}, R_{cryst}, and geometry parameters. Successive rounds of rebuilding and refinement were carried out to achieve the final R_{cryst}'s and R_{free}'s. Because *At*HPPD−869 and *At*HPPD−645 complexes were crystallized with the same monoclinic space group (*C*2) as *At*HPPD and had very similar unit cells, the rigid-body refinements were sufficient to locate the 3D positions of the protein structure of the complexes when the structure of *At*HPPD was used as the initial model. The ligand structures were modeled on the basis of inspection of $2F_o - F_c$ and $F_o - F_c$ electron density maps. Some adjustments to both the side and main chains were required to make a good match between the model and electron density map. The same procedures used in solving the *At*HPPD and *Rn*HPPD−869 structures were used to refine the *At*HPPD−869 and *At*HPPD−645 structures.

RESULTS AND DISCUSSION

Comparison with the Microbial HPPD Structure. Arabidopsis thaliana HPPD (*At*HPPD) was truncated at the N-terminus by 21 amino acids relative to the full-length sequence encoded by the cDNA (subsequent residue numberings reflect this truncation). This was done because we had previously determined that the N-terminus of HPPD purified from a native plant source (maize seedlings) was truncated relative to the full-length cDNA-encoded sequence (unpublished data). The truncated *At*HPPD was overexpressed in *E. coli* and purified to homogeneity. The structure of the purified enzyme was solved by multiple isomorphous replacement and refined to 1.8 Å (Table 1). The enzyme forms a homodimer (Figure 2a), whereas the *Pseudomonas fluorescens* (*Pf*HPPD) structure (Protein Data Bank code 1CJX) is homotetrameric (*11*). The eukaryotic enzyme exhibits two distinct structural domains, similar to the *Pf*HPPD topology, with an open twisted mixed and barrel-shaped β-sheet surrounded by α-helices.

A significant difference between the structures lies in the C-terminal helices. In *At*HPPD, the electron density for residues after Asn402 is not well defined, and even main chain atoms have high isotropic displacement parameters (>40 Å^2), whereas in *Pf*HPPD, this C-terminal helix is well defined with low isotropic displacement parameters (∼20−35 Å^2) for most of the atoms and fits more tightly with the core of the twisted β-barrel. *At*HPPD has a long and flexible loop (Val378 to Gly397) preceding the C-terminal helix with a disulfide bond between Cys380 and Cys395. This 19-

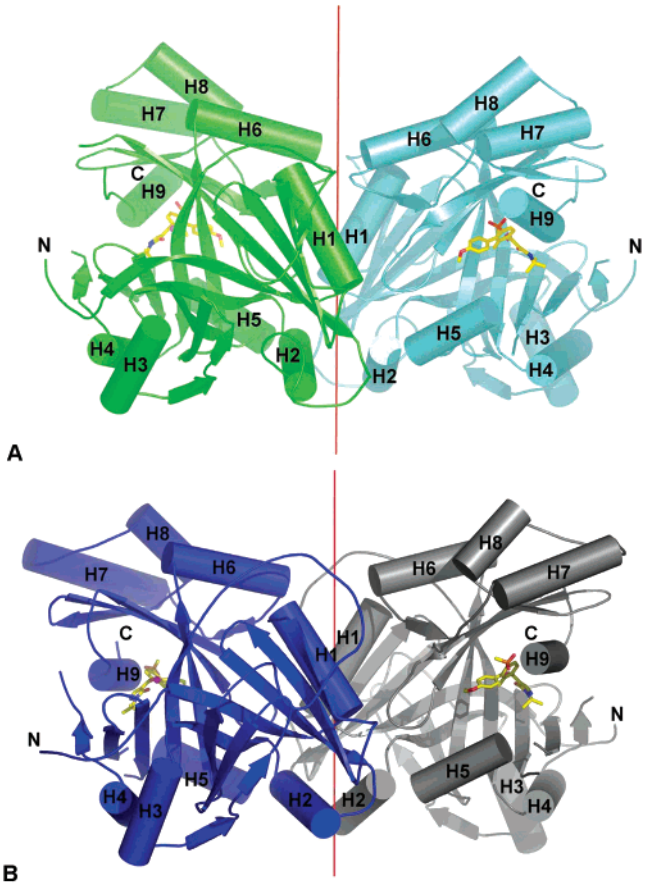

FIGURE 2: Ribbon diagram of the structures of (a) *At*HPPD−869 and (b) *Rn*HPPD−869 homodimer. The red axes represent the 2-fold rotation axis between the two monomers. The 2-fold axis in the *At*HPPD dimer is collinear with the crystallographic 2-fold axis. The axis in the *Rn*HPPD−869 dimer is a noncrystallographic 2-fold axis. The inhibitor DAS869 is located within each of the active sites and colored in the standard element colors. The nine α-helices are labeled H1−H9.

residue insertion appears to be unique to plant HPPDs based on sequence alignments comparing the currently available plant HPPD sequences with many sequences from other organisms. This loop is disordered such that electron density is often not evident for residues 383−389. The corresponding loop in *Pf*HPPD (Lys327 to Phe332) is significantly shorter and well defined and so may directly limit the possible orientations of the C-terminal helix. An additional difference near the active site between the plant and microbial structures is located in the β-sheet loop between Ala187 and Leu199 of *Pf*HPPD. These residues form two strands of β-sheet that loop over the top of the binding pocket and are close to the C-terminal helix. In *At*HPPD, this section (Ala230 to Gly243) is not resolved and may indicate that this binding site is more accommodating than that in *Pf*HPPD.

HPPD Active Site. The active site of *At*HPPD is located within an open twisted barrel-like β sheet. In common with other members of this dioxygenase family, the required metal ion at the catalytic center of the active enzyme is Fe^{2+}. This ion may not be tightly bound during purification because the purified enzyme had low activity without added Fe^{2+}. Because 3 mM cobalt chloride was present in our crystallization conditions and no exogenous iron was added, the metal ion at the active site in our crystals may be iron or cobalt. The oxidation state of the metal ion (+2 or +3) in the crystals is also not readily discerned. The iron found in the *Pf*HPPD crystals was determined to be in the ferric form (*11*). Because we cannot distinguish these two metal ions in our structures and do not have direct experimental evidence as to their oxidation states, we refer to the active site metal ion cofactor as M.

The metal ion in the *At*HPPD structure is coordinated by His205 (Nϵ2 atom), His287 (Nϵ2 atom), Glu373 (Oϵ1 atom), and three water molecules forming an octahedral complex (Figure 3a), in common with other members of the α-keto-glutarate-dependent dioxygenase family (*29*, *30*). *Pf*HPPD also has three residues (His161, His240, and Glu322) binding to the metal ion. The rms deviation of Cα of these three residues between the plant and microbial proteins is only 0.17 Å. However, the coordination found in *Pf*HPPD is in a distorted tetrahedral geometry with the fourth coordination site of *Pf*HPPD being provided by the oxygen atoms of an acetate molecule.

We first selected the inhibitor DAS869 (Figure 1) for cocrystallization with *At*HPPD as it is a potent inhibitor of both plant and rat HPPDs (I_{50} = 7 and <20 nM, respectively) and exhibits good herbicidal activity (*31*). DAS869 has bulky substituents relative to other HPPD inhibitors in our collection and so could potentially define the topography of the binding pocket to a greater extent. The structure of the plant enzyme−inhibitor complex (*At*HPPD−869) was solved by molecular replacement and refined to 1.8 Å resolution. The structure of *At*HPPD−869 was superimposed on that of *At*HPPD using the program O (*27*). The rms deviation was 0.38 Å over 364 Cα atoms. Inspection of the superimposed structures did not reveal any gross differences in the main chain atoms between the ligand-bound and unbound forms. The overall orientation of the inhibitor DAS869 within the active site pocket is shown in Figure 4.

In the enzyme−inhibitor complex, the three amino acids coordinating to the metal ion remain the same but two coordinating water molecules have been displaced by the 1,3-diketone moiety of the DAS869 inhibitor (Figure 3a,b). The distances from the oxygen atoms to the metal ion were refined to a range of 1.9−2.4 Å. This maintains the octahedral geometry and provides a strong ligand orientation and binding force. All potent HPPD inhibitors in the structural classes described to date contain an acidic 1,3-diketone moiety (*13*−*15*), and the coordination of both inhibitor oxygens to the active site metal ion is clearly an essential element for tight binding.

In addition to metal coordination, the inhibitor binding site involves the side chains of several residues, most notably the phenyl groups of Phe360 and Phe403, which form a π-stacking interaction with the benzoyl moiety of DAS869 (Figures 3b and 4). Phe403 is part of the C-terminal helix that remains unresolved after residue 402 in unliganded *At*HPPD. The presence of the ligand therefore appears to anchor this C-terminal helix resulting in good electron density visible out to Lys408. The N1-*tert*-butyl group on the ligand pyrazole has a tight fit against Pro259 and causes a shift of ~0.5 Å compared to its position in uncomplexed *At*HPPD. No hydrogen bonding interactions with the inhibitor were detected.

For a detailed comparison of inhibitor interactions between a plant and mammalian enzyme, the HPPD from rat (*Rn*HPPD) was cloned, overexpressed in *E. coli*, purified,

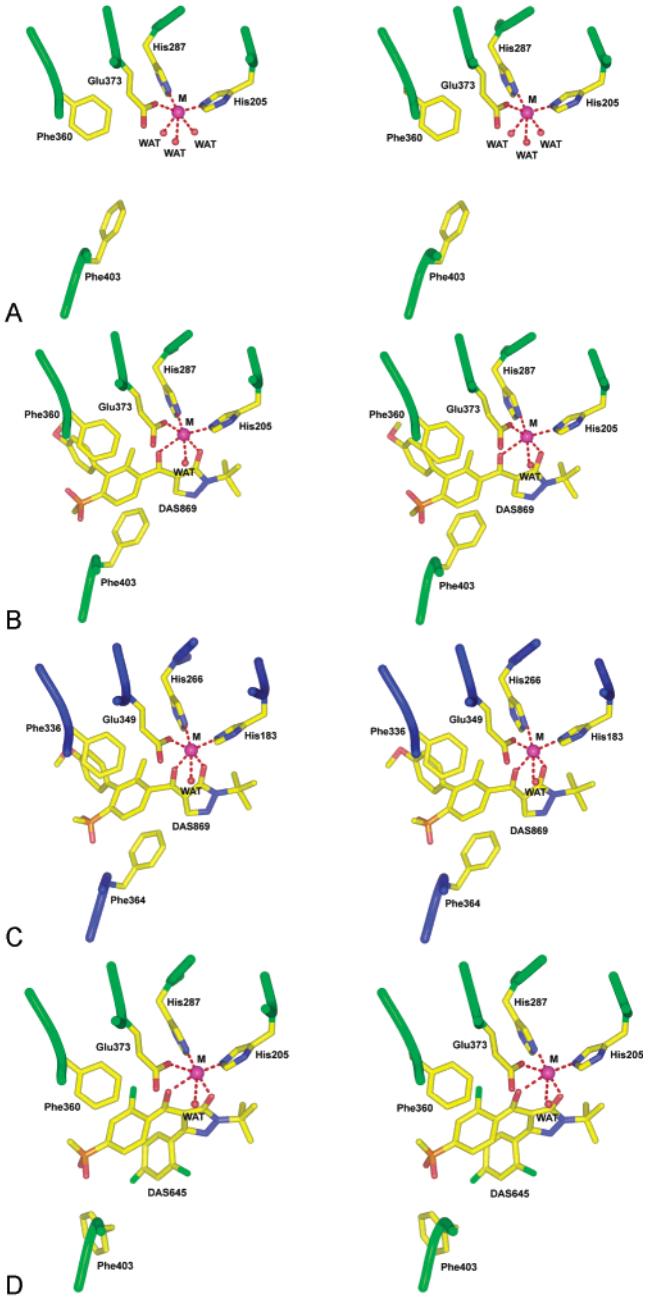

FIGURE 3: Stereodiagrams of the active sites of the (a) *At*HPPD, (b) *At*HPPD−869, (c) *Rn*HPPD−869, and (d) *At*HPPD−645 structures. Two histidine residues (His287 and His205 for *At*HPPD, His183 and His266 for *Rn*HPPD−869) and a glutamic acid residue (Glu373 for *At*HPPD, Glu349 for *Rn*HPPD−869) bind to the active site metal ion. Three water molecules also bind to the ion and form an octahedral coordination system. Two water molecules are displaced by the 1,3-diketone moiety from the inhibitor in the ligand-bound structures. Two phenylalanine residues (Phe360 and Phe403 in the *At*HPPD−869 structure, Phe336 and Phe364 in the *Rn*HPPD−869 structure) also form a π-stacking interaction with the inhibitor. The phenyl ring of Phe403 rotates away to avoid steric clash when DAS645 binds to the *At*HPPD active site.

and cocrystallized with DAS869 (*Rn*HPPD−869). *At*- and *Rn*HPPD have only 29% amino acid sequence identity, yet their overall structures are very similar (Figure 2). However, superimposition of the structures shows that there are some regions that do show some structural differences (Figure 5). The ligand binding features of *Rn*HPPD are very comparable to *At*HPPD−869 (Figure 3b,c). One prominent difference

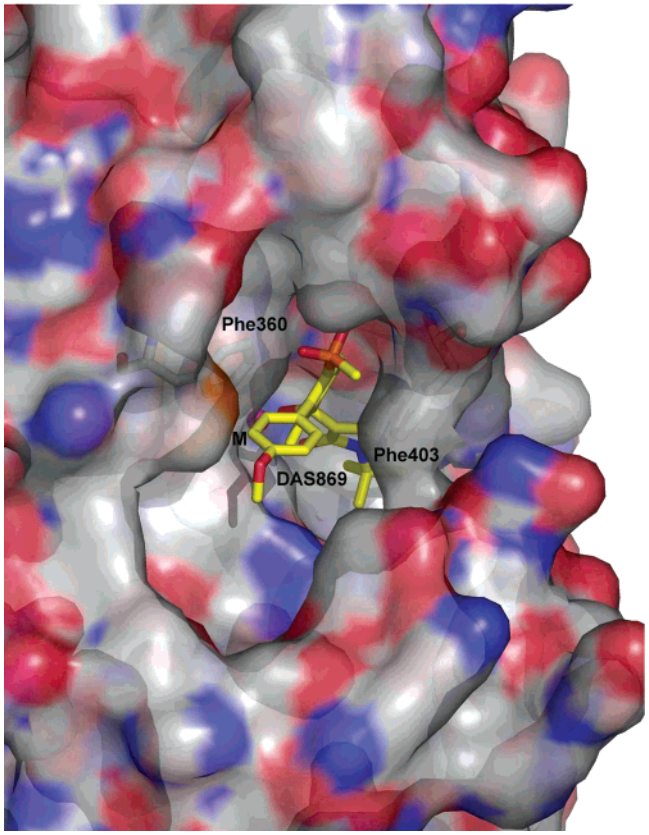

FIGURE 4: Active site pocket of *At*HPPD occupied by inhibitor DAS869. The metal ion coordinated by the inhibitor lies at the base of the pocket. The phenylalanine residues 360 and 403 that form a π-stacking interaction with the inhibitor are labeled.

occurs in the interaction of the N1-*tert*-butyl group of the inhibitor with Pro239 in *Rn*HPPD−869. Overlap of the protein backbones of the two structures indicates that Pro239 is not displaced in *Rn*HPPD−869 as was seen for Pro259 in *At*HPPD−869 (Figure 6); thus, this region is more restricted in the mammalian enzyme. Like the microbial *Pf*HPPD but unlike the plant *At*HPPD, the rat enzyme has a short rigid loop (His354 to Gly358) before the C-terminal helix, which may directly limit the flexibility and the possible orientations of the helix.

Plant-Selective HPPD Inhibitors. Detailed information on the relative selectivity of HPPD inhibitors has not been reported previously. We therefore screened a Dow AgroSciences collection of over 1000 HPPD inhibitors against both plant and mammalian HPPDs using a novel microplate-based assay of HPPD. A total of 950 of 1024 compounds tested had I_{50} values below 16 μM. The large majority of inhibitors tested were equipotent on the enzymes from both plant and mammalian sources, but six compounds were identified that showed significant selectivity (from 50 to >1600-fold) for inhibition of the plant enzyme. All six compounds had substitution patterns that included a phenyl substitution at C3, a *tert*-butyl substitution at N1 of the pyrazole ring, or both. DAS645 (Figure 1) contained both of these features and was remarkably selective for the plant enzyme. It had an I_{50} for *At*HPPD of 12 nM, whereas no significant inhibition of *Rn*HPPD could be detected at concentrations up to 20 μM DAS645 even with prolonged (3 h) incubation with the enzyme. The compound also had modest levels of herbicidal activity. This ligand was therefore

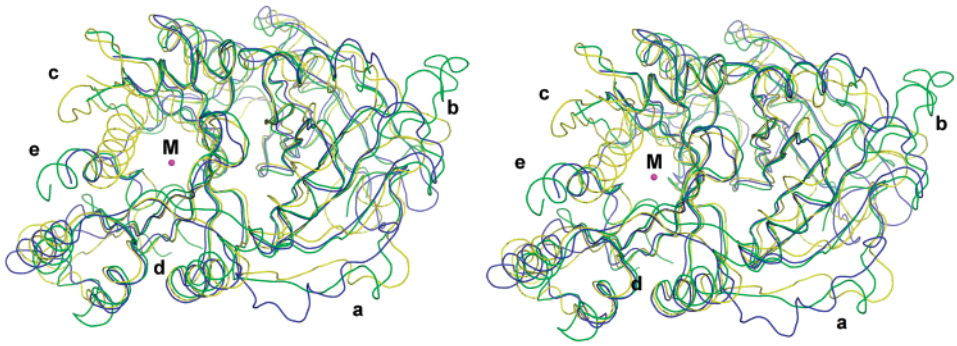

FIGURE 5: Stereodiagram of the superimposed HPPD structures of *At*HPPD (green), *Rn*HPPD−869 (blue), and *Pf*HPPD (yellow). The metal ion (M) in the active site is shown as a magenta sphere. Five significant structural differences between the plant and mammalian protein are labeled a−e. Regions a and b are located on the domain associated with the dimer interface, and regions c, d, and e are located in the domain containing the active site. The alignment was done using the program SQUOIA. *Rn*HPPD−869 and *Pf*HPPD were aligned against the *At*HPPD structure. The rms deviations were 2.6 Å over 330 Cα atoms for *Rn*HPPD−869 and 3.0 Å over 325 Cα atoms for *Pf*HPPD.

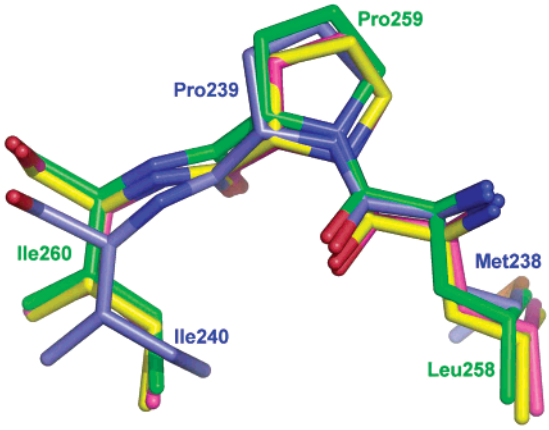

FIGURE 6: Superimposed views of Pro259 of *At*HPPD (green), *At*HPPD−869 (yellow), and *At*HPPD−645 (pink) and the equivalent Pro239 of *Rn*HPPD−869 (blue).

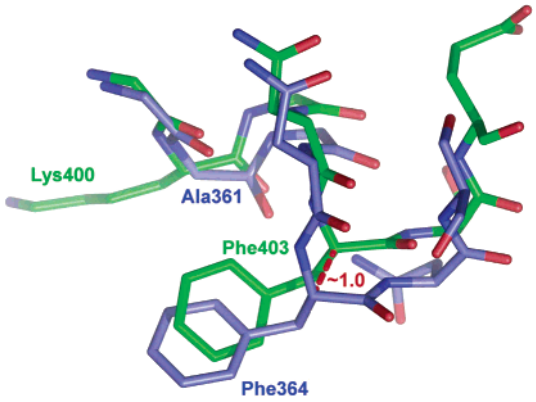

FIGURE 7: Superimposed C-terminal helices of *At*HPPD (green) and *Rn*HPPD−869 (blue) structures. The 1 Å displacement of the *At*HPPD Phe403 relative to *Rn*HPPD Phe364 is shown.

a useful compound to probe the structural basis of plant selectivity.

AtHPPD in Complex with a Plant-Selective Inhibitor. The structure of DAS645 in complex with *At*HPPD (*At*HPPD−645) was solved and refined to 1.9 Å resolution. The ligand binding site is similar to *At*HPPD−869 but with a few notable differences. One such difference is the positioning of the π-stacking network around the benzoyl moiety in *At*HPPD−645. Because of the steric presence of the 3-(2,4-dichlorophenyl) substitution on the pyrazole, Phe403 has rotated away from the inhibitor (Figure 3d). This significant movement of Phe403 was not seen in the structures of several enzyme−inhibitor complexes without the 3-phenyl pyrazole substitution (data not shown).

Another significant difference involves the positions of the C-terminal helix (residue 400 and above) of *At*HPPD, *At*HPPD−869, and *At*HPPD−645, which have created a slightly more open active site than the C-terminal helix in *Rn*HPPD−869. Thus, Phe403 is placed further from the center of the active site in the plant enzyme compared to the mammalian enzyme, which can allow larger inhibitor molecules to bind in the plant active site (Figure 7). This can be demonstrated with a quantitative assessment of the relative positions of the helices in the aligned structures. The structures of *At*HPPD−869, *At*HPPD−645, and *Rn*HPPD−869 were aligned with the *At*HPPD structure, and the rms deviations for the Cα atoms in each helix were calculated and listed in Table 2. The combined rms deviation for the 58 Cα atoms of the first six helices, H1−H6, which are remote from the binding site, are relatively low, under 0.093 Å for all *Arabidopsis* structures and 0.28 Å for the *Rn*-HPPD−869. For the seven Cα atoms of the C-terminal helix H9, however, the deviations are 0.11−0.23 Å for the *Arabidopsis* structures and 0.58 Å for *Rn*HPPD−869. Thus, the C-terminal helix is shifted relative to the first six helices in all the structures, but especially in the *Rn*HPPD−869 structure.

The rat enzyme contains a short five-residue turn (His354 to Gly-358) preceding the C-terminal helix, similar to the *Pf*HPPD enzyme, whereas the *Arabidopsis* enzyme contains a unique long disordered loop (Val378 to Gly397). The *At*HPPD sequence also contains Gly-Gly pairs before and after Cys395, just before the start of the C-terminal helix, that are not present in the rat sequence and could act as hinge regions. Thus, the C-terminal helix of *At*HPPD appears to be slightly hinged to the protein, whereas that of the *Rn*HPPD is not.

In both the plant and mammalian HPPD structures, the C-terminal helix packs against another helix, H7. This is preceded in the *Arabidopsis* enzyme by a five-residue segment that contains four prolines (^{315}PSPPP^{319}), whereas in the rat enzyme, helix H7 is preceded by ^{290}AVPS^{293}. This difference leads to the helix H7 of *At*HPPD being dislocated relative to that of the *Rn*HPPD−869 structure. Quantitatively, the rms deviation of the nine Cα atoms of *Rn*HPPD−869 is

Table 2: Comparison of rms Deviations of the Cα Atoms of Helices in Ligand-Bound HPPD Structures Aligned with Unliganded *At*HPPD

Sequences of helices Arabidopsis HPPD Rat HPPD	**R.m.s. deviation relative to AtHPPD structure (Å)**		
	AtHPPD-645	**AtHPPD-869**	**RnHPPD-869**
^{37}TNVARRFSWG^{46}...^{106}SCRSFFSS^{113}...^{128}AESAFSISVA^{137}... ^{30}KQAASFYCNK^{39}... ^{81}EMGDHLVK^{88}... ^{103}CEHIVQKARE^{112}... ^{214}GPALTYVAGFT^{224}...^{272}QIQTYLEHN^{280}...^{295}IFRTLREMRK^{304} ^{194}ESASEWYLKNL^{204}...^{251}QIQEYVDYN^{259}...^{274}IITTIRHLRE^{283}	0.093	0.074	0.28
^{320}TYYQNLKKR^{328} ^{294}SYYRLLKQN^{302}	0.28	0.17	1.15
^{337}QIKECEEL^{344} ^{313}DMDVLEEL^{320}	0.24	0.081	0.28
^{399}GKGNFSE^{405} ^{360}GAGNFNS^{366}	0.11	0.23	0.58

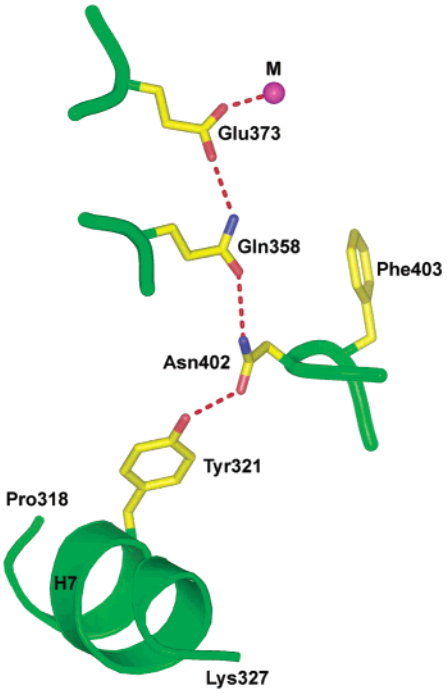

FIGURE 8: Hydrogen bond chain observed near the active site of *At*HPPD−869 linking helix 7 with the active site metal ion through three hydrogen bonds. Phe403 forms a π-stacking interaction with the bound inhibitor. A similar hydrogen bond chain via equivalent residues is found in the *Rn*HPPD−869 structure.

relatively high, 1.15 Å (Table 2). This may account for the differing positions of the C-terminal helix between plant and mammalian structures.

A network of hydrogen bonds was noted near the C-terminus and active sites of both *At*HPPD and *Rn*HPPD−869 consisting of Tyr321, Gln358, Glu373 (M ligand), and Asn402 in the plant enzyme (Figure 8) and Tyr295, Gln334, Glu349 (M ligand), and Asn363 in the rat enzyme. The tyrosine residue (from helix H7) forms a direct H-bond with the asparagine from H9 and can greatly restrict the position of the key adjacent phenylalanine residue (*At*HPPD Phe403, *Rn*HPPD Phe364.) The rat enzyme C-terminal helix is held closer to the active site than the plant enzyme C-terminal helix resulting in Cα and Cβ atoms of Phe364 of the rat enzyme being about 1 Å closer to its active site than those of Phe403 in *At*HPPD (Figure 7). In order for DAS645 to bind to the rat enzyme, its 3-(2,4-dichlorophenyl) ring would inevitably be much closer to the Cβ atom of Phe364 than it actually is to the Cβ of Phe403 in plant enzyme. The C-terminal helix of rat enzyme would therefore have to move considerably to accommodate the substituted phenyl ring of the inhibitor. This helix rearrangement may be difficult to achieve in the rat enzyme because of the short unhinged turn preceding this helix and the H-bond chain mentioned above. This could explain why DAS645 has very high affinity for the plant enzyme yet undetectable inhibition of the rat enzyme.

An additional contribution to selectivity apparently occurs in a separate region of the active site. Ligands containing an N1-*tert*-butylpyrazole, such as DAS645 and DAS869, displace the Pro259 ring atoms distally by about 0.5 Å compared to their position in the native *At*HPPD structure. In *Rn*HPPD−869, it appears that the equivalent Pro239 cannot be readily repositioned, leaving the region slightly more restricted and the ligand binding site smaller in the rat enzyme (Figure 6). The *Rn*HPPD Pro239 is held in place by adjacent residue Met238. The side chain of this residue is longer than the corresponding plant residue Leu258 and is already tightly packed against the core of highly stable residues such as Ile96, Tyr139, and Tyr200. The main chain of the H4 helix in the rat enzyme prohibits movement of the other adjacent residue Ile240 in a similar fashion. These steric barriers prevent the rat Pro239 from shifting like the plant Pro259. The rat enzyme must accommodate the N1-*tert*-butyl group of DAS869 by a displacement of the inhibitor toward the center of the ligand binding site instead.

Summary of Basis for Inhibitor Selectivity. Combining the three key structural differences that were observed, we propose a rationale for the plant selectivity of DAS645 and other plant-selective inhibitors of HPPD. In *At*HPPD−869, Phe403 is further away from the metal ion binding site than corresponding Phe364 in *Rn*HPPD−869. *At*HPPD also has

a more flexible C-terminal helix and more movable Pro259 than the rat enzyme. An inhibitor such as DAS645, containing both an N1-*tert*-butyl group and a substituted 3-phenyl pyrazole, is able to bind to the metal ion while avoiding steric clashes by relocating Phe403 and displacing Pro259 distally, accommodating the bulky inhibitor in the plant enzyme. In contrast, this same inhibitor will collide with the *Rn*HPPD Phe364 because the inhibitor is displaced toward Phe364 and away from Pro239, while the Phe364 cannot rearrange due to C-terminal helix inflexibility. The size, geometry, and substitution patterns of the inhibitor are key factors in generating its selectivity and these steric barriers can reduce the binding affinity dramatically.

This study has provided a detailed visualization of inhibitor binding to HPPDs from both plant and mammalian sources so provides a new and useful basis for the design of novel herbicides and drugs targeted at HPPD. Our discovery of highly selective inhibitors of the plant enzyme and the subsequent insights into the structural basis of plant selectivity offer unique and powerful tools for the design of agrochemicals with improved toxicological profiles. Similar studies combining detailed structural information with the results from screens for selective inhibitors using other target sites may enable a wider variety of targets that are shared by both pests and vertebrates to be exploited for safer and more effective chemical crop protection.

ACKNOWLEDGMENT

Thanks to Tim Hey, Susan Green, and Ignacio Larrinua for assistance with cloning and expression of HPPDs, Jodi DeSchepper for technical assistance in crystallizations, and Tim Rydel for initial help in the project.

REFERENCES

1. Pallett, K. E., Little, J. P., Sheekey, M., and Veerasekaran, P. (1998) The mode of action of isoxaflutole I. physiological effects, metabolism, and selectivity, *Pestic. Biochem. Physiol. 62*, 113−124.
2. Mitchell, G., Bartlett, D. W., Fraser, T. E. M., Hawkes, T. R., Holt, D. C., Townson, J. K., and Wichert, R. A. (2001) Mesotrione: a new selective herbicide for use in maize, *Pest Manage. Sci. 57*, 120−128.
3. Cerone, R., Holme, E., Schiaffino, M. C., Caruso, U., Maritano, L., and Romano, C. (1997) Tyrosinemia type III: diagnosis and ten-year follow-up, *Acta Paediatr. 86*, 1013−1015.
4. Endo, F., Kitano, A., Uehara, I., Nagata, N., Matsuda, I., Shinka, T., Kuhara, T., and Matsumoto, I. (1983) Four-hydroxyphenylpyruvic acid oxidase deficiency with normal fumarylacetoacetase: a new variant form of hereditary hypertyrosinemia, *Pediatr. Res. 17*, 92−96.
5. Sanchez-Amat, A., Ruzafa, C., and Solano, F. (1998) Comparative tyrosine degradation in *Vibrio cholerae* strains. The strain ATCC 14035 as a prokaryotic melanogenic model of homogentisate-releasing cell, *Comp. Biochem. Biophys. B119*, 557−562.
6. Tomoeda, K., Awata, H., Matsuura, T., Matsuda, I., Ploechl, E., Milovac, T., Boneh, A., Scott, C. R., Danks, D. M., and Endo, F. (2000) Mutations in the 4-hydroxyphenylpyruvic acid dioxygenase gene are responsible for tyrosinemia type III and hawkinsinuria, *Mol. Genet. Metab. 71*, 506−510.
7. Holme, E., and Lindstedt, S. (1998) Tyrosinaemia type I and NTBC (2-(2-nitro-4-trifluoromethylbenzoyl)-1,3-cyclohexanedione), *J. Inherited Metab. Dis. 21*, 507−517.
8. Norris, S. R., Barrette, T. R., and DellaPenna, D. (1995) Genetic dissection of carotenoid synthesis in Arabidopsis defines plastoquinone as an essential component of phytoene desaturation, *Plant Cell 7*, 2139−2149.
9. Ryle, M. J., and Hausinger, R. P. (2002) Non-heme iron oxygenases, *Curr. Opin. Chem. Biol. 6*, 193−201.
10. Crouch, N. P., Adlington, R. M., Baldwin, J. E., Lee, M. H., and Mackinnon, C. H. (1997) A mechanistic rationalization for the substrate specificity of recombinant mammalian 4-hydroxyphenylpyruvate dioxygenase (4-HPPD), *Tetrahedron 53*, 6993−7010.
11. Serre, L., Sailland, A., Sy, D., Boudec, P., Rolland, A., Pebay-Peyroula, E., and Cohen-Addad, C. (1999) Crystal structure of *Pseudomonas fluorescens* 4-hydroxyphenylpyruvate dioxygenase: an enzyme involved in the tyrosine degradation pathway, *Structure 7*, 977−988.
12. Fritze, I. M., Linden, L., Freigang, J., Auerbach, G., Huber, R., and Steinbacher, S. (2004) The crystal structures of *Zea mays* and *Arabidopsis* 4-hydroxyphenylpyruvate dioxygenase, *Plant Physiol. 134*, 1388−1400.
13. Pallett, K. E., Cramp, S. M., Little, J. P., Veerasekaran, P., Crudace, A. J., and Slater, A. E. (2001) Isoxaflutole: the background to its discovery and the basis of its herbicidal properties, *Pest Manage. Sci. 57*, 133−142.
14. Lee, D. L., Knudsen, C. G., Michaely, W. J., Chin, H. L., Nguyen, N. H., Carter, C. G., Cromartie, T. H., Lake, B. H., Shribbs, J. M., and Fraser, T. (1998) The structure−activity relationships of the triketone class of p-hydroxyphenylpyruvate dioxygenase inhibiting herbicides, *Pestic. Sci. 54*, 377−384.
15. Meazza, G., Scheffler, B. E., Tellez, M. R., Rimando, A. M., Romagni, J. G., Duke, S. O., Nanayakkara, D., Khan, I. A., Abourashed, E. A., and Dayan, F. E. (2002) The inhibitory activity of natural products on plant p-hydroxyphenylpyruvate dioxygenase, *Phytochemistry 60*, 281−288.
16. Garcia, I., Job, D., and Matringe, M. (2000) Inhibition of p-hydroxyphenylpyruvate dioxygenase by the diketonitrile of isoxaflutole: A case of half-site reactivity, *Biochemistry 39*, 7501−7507.
17. Ellis, M. K., Whitfield, A. C., Gowans, L. A., Auton, T. R., Provan, W. M., Lock, E. A., Lee, D. L., and Smith, L. L. (1996) Characterization of the interaction of 2-[2-Nitro-4-(trifluoromethyl)benzoyl]-4,4,6,6-tetramethylcyclohexane-1,3,5-trione with rat hepatic 4-hydroxyphenylpyruvate dioxygenase, *Chem. Res. Toxicol. 9*, 24−27.
18. Kavana, M., and Moran, G. R. (2003) Interaction of (4-hydroxyphenyl)pyruvate dioxygenase with the specific inhibitor 2-[2-nitro-4-(trifluoromethyl)benzoyl]-1,3-cyclohexanedione, *Biochemistry 42*, 10238−10245.
19. Neidig, M. L., Kavana, M., Moran, G. R., and Solomon, E. I. (2004) CD and MCD studies of the non-heme ferrous active site in (4-hydroxyphenyl)pyruvate dioxygenase: Correlation between oxygen activation in the extradiol and α-kg-dependent dioxygenases, *J. Am. Chem. Soc. 126*, 4486−4487.
20. Lock, E. A., Ellis, M. K., Gaskin, P., Robinson, M., Auton, T. R., Provan, W. M., Smith, L. L., Prisbylla, M. P., Mutter, L. C., and Lee, D. L. (1998) From toxicological problem to therapeutic use: The discovery of the mode of action of 2-(2-nitro-4-trifluoromethylbenzoyl)-1,3-cyclohexanedione (NTBC), its toxicology and development as a drug, *J. Inherited Metab. Dis. 21*, 498−506.
21. Lee, D. L., Prisbylla, M. P., Cromartie, T. H., Dagarin, D. P., Howard, S. W., Provan, W. M., Ellis, M. K., Fraser, T., and Mutter, L. C. (1997) The discovery and structural requirements of inhibitors of p-hydroxyphenylpyruvate dioxygenase, *Weed Sci. 45*, 601−609.
22. Studier, F. W., Rosenberg, A. H., Dunn, J. J., and Dubendorff, J. W. (1990) Use of T7 RNA polymerase to direct expression of cloned genes, *Methods Enzymol. 185*, 60−89.
23. Secor, J. (1994) Inhibition of barnyardgrass 4-hydroxyphenylpyruvate dioxygenase by sulcotrione, *Plant Physiol. 106*, 1429−1433.
24. Schmidt, S. R., Mueller, C. R., and Kress, W. (1995) Murine liver homogentisate 1,2-dioxygenase. Purification to homogeneity and novel biochemical properties, *Eur. J. Biochem. 228*, 425−430.
25. Pflugrath, J. W. (1999) The finer things in X-ray diffraction data collection, *Acta Crystallogr. D55*, 1718−1725.
26. Bailey, S. (1994) The CCP4 suite: programs for protein crystallography, *Acta Crystallogr. D50*, 760−763.
27. Jones, T. A., Zhou, J. Y., Cowan, S. W., and Kjeldgaard, M. (1991) Improved methods of building protein models in electron density maps and the location errors in these methods, *Acta Crystallogr. A47*, 110−119.
28. Yang, C., and Pflugrath, J. W. (2001) Applications of anomalous scattering from S atoms for improved phasing of protein diffraction data collected at Cu Ka wavelength, *Acta Crystallogr. D57*, 1480−1490.
29. Valegard, K., Terwisscha van Scheltinga, A. C., Lloyd, M. D., Hara, T., Ramaswamy, S., Perrakis, A., Thompson, A., Lee, H.

J., Baldwin, J. E., Schofield, C. J., Hajdu, J., and Andersson, I. (1998) Structure of a cephalosporin synthase, *Nature 394*, 805−809.

30. Zhang, Z., Ren, J., Stammers, D. K., Baldwin, J. E., Harlos, K., and Schofield, C. J. (2000) Structural origins of the selectivity of the trifunctional oxygenase clavaminic acid synthase, *Nat. Struct. Biol. 7*, 127−133.

31. Siddall, T. L., Ouse, D. G., Benko, Z. L., Garvin, G. M., Jackson, J. L., McQuiston, J. M., Ricks, M. J., Thibault, T. D., Turner, J. A., Vanheertum, J. C., and Weimer, M. R. (2003) Synthesis and herbicidal activity of phenyl-substituted benzoylpyrazoles, *Pest Manage. Sci. 58*, 1175−1186.

BI049323O